

Multiwavelength monitoring of a very active dwarf nova AX J1549.8–5416 with an unusually high duty cycle

Guobao Zhang^{1*}, Joseph D. Gelfand^{1,2}, David M. Russell¹, Fraser Lewis^{3,4}
Nicola Masetti^{5,6}, Federico Bernardini¹, Ileana Andruchow^{7,8} and L. Zibecchi^{7,8}

¹New York University Abu Dhabi, P.O. Box 129188, Abu Dhabi, UAE

²Center for Cosmology and Particle Physics, New York University, Meyer Hall of Physics, 4 Washington Place, New York, NY 10003

³Faulkes Telescope Project, School of Physics and Astronomy, Cardiff University, 5 The Parade, Cardiff, CF24 3AA, Wales, UK

⁴Astrophysics Research Institute, Liverpool John Moores University, IC2, Liverpool Science Park, 146 Brownlow Hill, Liverpool L3 5RF, UK

⁵INAF – Istituto di Astrofisica Spaziale e Fisica Cosmica di Bologna, via Gobetti 101, 40129 Bologna, Italy

⁶Departamento de Ciencias Físicas, Universidad Andrés Bello, Fernández Concha 700, Las Condes, Santiago, Chile

⁷Facultad de Ciencias Astronómicas y Geofísicas, Universidad Nacional de La Plata, Paseo del Bosque, B1900FWA La Plata, Argentina

⁸Instituto de Astrofísica La Plata (IALP), CONICET-UNLP, Argentina

31 July 2018

ABSTRACT

We present the results of our analysis of new optical, ultraviolet (UV) and X-ray observations of a highly variable source – AX J1549.8–5416. Both the detection of several fast rise, exponential decay outbursts in the optical light curve and the lack of He II emission lines in the optical spectra suggest AX J1549.8–5416 is a cataclysmic variable of the dwarf nova (DN) type. The multiwavelength analysis of three mini-outbursts and one normal outburst represent one of the most complete multiwavelength studies of a DN and help to refine the relationship between the X-ray, UV and optical emission in this system. We find that the UV emission is delayed with respect to the optical by 1.0–5.4 days during the rising phase of the outburst. The X-ray emission is suppressed during the peak of the optical outburst and recovers during the end of the outburst. From our analysis of archival *Swift*, *Chandra* and *XMM-Newton* observations of AX J1549.8–5416, we estimate this DN has a high duty cycle ($\sim 50\%$), suggesting a quiescent X-ray luminosity larger than 10^{32} erg/s. We also find the X-ray and UV flux are roughly anti-correlated. Furthermore, we find that, at low X-ray fluxes, the X-ray spectrum is well described by a single temperature thermal plasma model, while at high X-ray fluxes, an isobaric cooling flow model also works. We find that the maximum temperature of the plasma in quiescence is significantly higher than that in outburst.

Key words: stars: dwarf novae — X-rays: binaries — stars: individual: AX J1549.8–5416

1 INTRODUCTION

Cataclysmic variables (CVs) are interacting binaries consisting of a low-mass secondary star very close to a more massive white dwarf (WD) primary star. The WD accretes matter from the companion star via Roche lobe overflow. CVs are classified into several types based on their observational characteristics, depending on the nature of the primary star and the accretion process (see reviews by Kuulkers et al. 2006; Singh 2013). In particular, CVs are divided into non-magnetic CVs (non-MCVs) and magnetic CVs (MCVs) based on the strength of the WD surface magnetic field. In

non-MCVs, X-rays are thought to originate from the boundary layer (BL) between the slowly rotating accreting WD and the fast rotating (Keplerian) inner edge of the accretion disc, where the material dissipates its remaining rotational kinetic energy before accreting onto the surface of the WD. In MCVs, X-rays originate from an accretion column at or near the magnetic poles. The columns may be fed via magnetospheric accretion from the inner boundary of a truncated disc, as in the subclass of intermediate polars (IPs), or from a funneled accretion stream in polars. The X-ray spectra of magnetic and non-magnetic CVs are typically described by multi-temperature thermal plasma emission (e.g., Kuulkers et al. 2006; Singh 2013).

* E-mail: guobao.zhang@nyu.edu

Dwarf novae (DNe) are non-MCVs with an accretion

disc that flows onto the WD primary, and a secondary star. The orbital periods of DNe are typically between 70 minutes and 10 hours (Kuulkers et al. 2006; Patterson 2011; Balman 2012). In DNe, the accretion disc has two stable states which correspond to optical quiescence and outbursts. During optical quiescence, the X-ray emission arises from the hot, optically thin, thermal plasma produced at the BL. The X-ray spectrum is hard, has a temperature greater than 10 keV, and typically features associated with the Fe K_{α} line are observed. Furthermore, during this state the optically thick accretion disc is truncated, and the accretion rate is less than $10^{-9} - 10^{-9.5} M_{\odot}/\text{year}$.

When in outburst, the optical flux increases by 2–9 magnitudes for several days to weeks. This increase is associated with an increase in the luminosity of the accretion disc which dominates the emission at optical and UV wavelengths (e.g., Lasota 2001; Kuulkers et al. 2006). During this period, the X-ray spectra is soft, and the plasma temperature decreases such that the thermal emission peaks in the extreme UV. Due to the increase in accretion rate on the WD, the plasma in the BL becomes optically thick and therefore more efficient at cooling (Pandel et al. 2003; Saitou et al. 2012; Baskill et al. 2005; Collins & Wheatley 2010; McGowan et al. 2004). The mechanism leading to repeated transitions between the optical outburst and quiescent states is thought to be thermal viscous disc instability (e.g., Meyer & Meyer-Hofmeister 1981; Lasota 2001).

An analysis of archival *Swift* data identified a highly variable X-ray source – AX J1549.8–5416 – which was first detected in the ASCA Galactic plane Survey (Sugizaki et al. 2001). Its optical counterpart was proposed to be NSV 20407, a variable star with a B-band magnitude ranging from > 18 to 16.7 (Samus et al. 2009), suggesting this source is a CV. Lin et al. (2014) analysed four *XMM-Newton* observations of AX J1549.8–5416 and found that the source’s X-ray flux varied considerably. They also detected a Fe line in the X-ray spectra of two observations and suggested this source be a MCV, which often have Fe emission in their X-ray spectra (Ezuka & Ishida 1999).

In order to further investigate the nature of AX J1549.8–5416, we observed the source at optical wavelengths with the Las Cumbres Observatory Global Telescope Network (LCOGT) and ‘Jorge Sahade’ at CASLEO (Argentina), complemented with UV and X-ray observations by *Swift*. Since AX J1549.8–5416 is located ~ 9.2 arcmin away from 1E 1547.0–5408, it is within the field of view of a large number of archival *Swift* observations. In this paper, we also analysed all available archival *XMM-Newton*, *Chandra*, and *Swift* data of the source. We describe the observations and data reduction in Section 2, and we present our results in Section 3. Finally, in Section 4 we discuss our findings and summarize our conclusions in Section 5.

2 OBSERVATIONS AND DATA REDUCTION

2.1 LCOGT Optical observations

We observed the field of AX J1549.8–5416 with the LCOGT suite of robotic 1-m telescopes, from 2015-04-30 to 2015-06-18 and from 2016-02-01 to 2016-04-30. Some data in 2016 were taken with the 2-m Faulkes Telescope South (FTS).

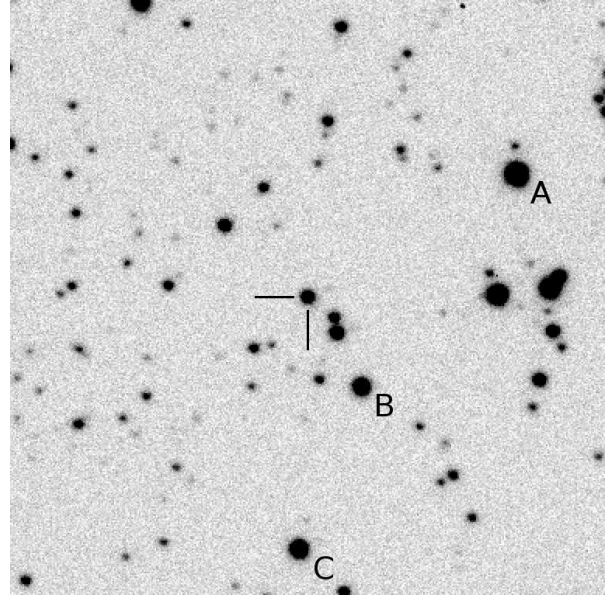


Figure 1. Optical (*R*-band, taken on 2015-06-10 at Cerro Tololo) finding chart. The field of view is 3.0×3.0 arcmin; north is up and east is to the left. AX J1549.8–5416 is marked at the centre, and the stars A, B and C are the three used for flux calibration.

These data were acquired as part of our Faulkes Telescopes monitoring project of X-ray transients (Lewis et al. 2008). Optical images were acquired in four filters: Bessel *B*-band, *V*-band, *R*-band and SDSS *i'*-band. The observation logs are provided in Table A1. All LCOGT telescopes are equipped with a camera with pixel scale $0.467 \text{ arcsec pixel}^{-1}$, while the camera of FTS has $0.301 \text{ arcsec pixel}^{-1}$. Bias subtraction and flat-fielding were performed via the automatic pipelines¹.

The optical counterpart of AX J1549.8–5416 is clearly visible, at a location consistent with the position of the X-ray source, the UV source and the known variable star NSV 20407. Photometry was performed on the target and three field stars in the APASS data release 9 catalogue (Henden et al. 2015, see Fig. 1) using PHOT in IRAF, adopting a 2.8 arcsec aperture. We calibrated the field using the catalogue *B*, *V* and *i'*-band magnitudes of the three field stars, which have typical errors of 0.01–0.1 mag. *R*-band flux calibration was achieved using the transformation from *V*, *r'* and *i'*-bands described by Jordi et al. (2006).

For the first four observations, all four filters were used to constrain the colour and variability amplitude of the source. Variations of amplitude ~ 2 mag were seen in all bands, and for subsequent observations just *R*-band was used (see Table A1 for details). As a check of our relative errors, photometry was performed on a fourth field star in *R*-band. Its magnitude differed from its mean value of $R = 16.11$ mag by $< 2\sigma$ in 25 of 26 images in 2015. The mean error on the magnitude of this field star measured from each image was 0.03 mag, and for AX J1549.8–5416 the mean magnitude errors were 0.10, 0.05, 0.04 and 0.04 mag in *B*, *V*, *R* and *i'*-bands, respectively. The image quality was particularly bad in the observation taken on 2015-06-18, which

¹ <https://lcogt.net/observatory/data/BANZAIPipeline>

Table 1. New *Swift*/XRT observations. The error bars are given in 1- σ level.

ObsID	Date UT	MJD	exposure (s)	X-ray rate ($\times 10^{-3}$ cnt/s)	UV magnitude	UVOT filter
00042706002	2016-02-11T17:40:32	57429.73648148	685	6.09 ± 3.04	> 20.3	uvw2
00042706003	2016-02-15T22:14:32	57433.92675926	505	4.19 ± 2.96	19.37 ± 0.2	uvw2
00042706004	2016-02-19T15:25:11	57437.64248843	585	31.61 ± 7.45	19.31 ± 0.18	uvw2
00042706005	2016-02-24T22:58:47	57442.95748843	850	16.94 ± 4.52	19.22 ± 0.18	uvm2
00042706006	2016-02-27T11:48:53	57445.49228009	775	13.17 ± 4.16	20.04 ± 0.29	uvw2
00042706007	2016-03-04T04:42:00	57451.19583333	1135	7.19 ± 2.54	19.11 ± 0.12	uvw1
00042706008	2016-03-14T20:13:22	57461.84322042	995	3.08 ± 1.78	19.21 ± 0.13	uvw2
00042706009	2016-03-18T04:11:02	57465.17493410	810	1.25 ± 1.25	18.89 ± 0.13	uvw2
00042706010	2016-03-25T08:07:36	57472.33861111	1020	13.11 ± 3.63	18.50 ± 0.15	u
00042706011	2016-03-28T01:36:03	57475.06670139	895	11.31 ± 3.57	19.04 ± 0.14	uvw1
00042706012	2016-03-31T21:52:52	57478.91171296	965	22.07 ± 4.81	> 20.28	uvm2
00042706013	2016-04-03T01:12:19	57481.05021991	1000	19.41 ± 4.45	> 20.37	uvw2
00042706014	2016-04-06T12:13:08	57484.50912037	890	6.92 ± 2.82	> 20.41	u)
00042706015	2016-04-09T10:27:51	57487.43600694	485	2.07 ± 1.99	16.33 ± 0.04	uvw1
00042706016	2016-04-10T19:56:28	57488.83167344	472	6.35 ± 3.67	15.82 ± 0.03	u
00042706016	—	—	—	—	16.88 ± 0.09	uvw2
00042706017	2016-04-16T22:34:05	57494.94112905	830	—	17.94 ± 0.08	uvm2
00042706018	2016-04-19T22:27:44	57497.93672437	945	—	18.85 ± 0.20	uvw2
00042706019	2016-04-22T08:58:27	57500.37471492	904	9.60 ± 3.32	18.17 ± 0.06	u
00042706020	2016-04-25T23:17:06	57503.97099751	670	10.14 ± 3.95	19.86 ± 0.29	uvw1

resulted in a larger magnitude error. On 2015-06-10, 20 *R*-band images were taken to search for short-term variability. The results are shown in Section 3.1. In 2016 we carried out a high cadence monitoring campaign in *R*-band to closely follow the morphology and evolution of a full outburst.

2.2 CASLEO optical observations

Optical spectra of NSV 20407, the optical counterpart of AX J1549.8–5416, were acquired using the 2.15-m ‘Jorge Sahade’ telescope at CASLEO (Argentina). This telescope is equipped with a REOSC spectrograph, which carries a 1024×1024 pixel TEK CCD. The spectra were acquired in Simple Dispersion mode using the #270 grism (300 lines/mm) and a 2'' slit width, allowing one to nominally cover the 3500–7500 Å spectral range with a dispersion of 3.4 Å pixel⁻¹.

Two 1200-s spectroscopic frames were secured on 2015 April 14, with start times of 04:54 and 05:16 UT, respectively. After cosmic ray rejection, the spectra were reduced, background subtracted and extracted (Horne 1986) using IRAF² (Tody 1993). Wavelength calibration was performed using Cu-Ne-Ar lamps acquired before each spectroscopic exposure; the spectra were then flux-calibrated using the spectrophotometric standard LTT 6284 (Hamuy et al. 1994). Finally, the two spectra were stacked together to increase the signal-to-noise ratio. The wavelength calibration uncertainty was ~ 0.5 Å; this was checked using the positions of background night sky lines.

2.3 Swift observations

We analysed all available observations since 2007 June 2 (including archival and new observations that we requested),

² Image Reduction and Analysis Facility (IRAF) is available at <http://iraf.noao.edu/>

taken in Photon Counting (PC) mode with the X-Ray Telescope (XRT; Burrows et al. 2005) on board the *Swift* satellite. The XRT observations with exposure times longer than 500s were reduced using the *Swift* tools within the *heasoft* v. 6.16 (Blackburn 1995) software package. Source detection and position determination were carried out using the recipes described in Evans et al. (2009). The source light curves and spectra were extracted in the 0.5–10.0 keV band using a circular extraction region with a radius of 20 arcsec centred on the position of the source. Background data were extracted from an annular region with an inner (outer) radius of 30 arcsec (60 arcsec). The 19 new *Swift* observations are shown in Table 1.

Since AX J1549.8–5416 is not at the center source of the archival *Swift* observations and the UVOT field of view is smaller than XRT, the source was not observed in all UVOT observations. We reduced all available UVOT observations which contained this source in the field. In each UVOT observation, this source was observed with at least one of the four filters with corresponding central wavelengths (Poole et al. 2008): uvw2 (1928 Å) uvm2 (2246 Å), uvw1 (2600 Å), and u (3465 Å). The UVOT data were analysed following the methods of Poole et al. (2008) and Brown et al. (2009).

2.4 XMM-Newton observations

We analysed five *XMM-Newton* observations of the source between February 2004 and February 2010. We reduced the *XMM-Newton* Observation Data Files (ODF) using version 12.0.1 of the Science Analysis Software (SAS). We used the EPPROC task to extract the event files for the PN camera. Source light curves and spectra were extracted in the 0.5–10.0 keV band using a circular extraction region with a radius of 20 arcsec centred on the position of the source. Background light curves and spectra were extracted from a circular source-free region of radius 30 arcsec on the same CCD. We applied standard filtering and examined the light

Table 2. The *XMM-Newton* and *Chandra* observations in which the source was detected. The source net count rates were calculated in the 0.3–10 keV energy band converted using PIMMS. Errors represent the 90% confidence level. We converted the *XMM-Newton* and *Chandra* count rate to equivalent *Swift*-XRT count rates. The last column shows the 3- σ upper limit of the pulsed fraction for each observation.

Instr.	No.	ObsID	Date	Exp. ks	Rate 10^{-2} counts s^{-1}	Rate(XRT/PC) 10^{-3} counts s^{-1}	pulsed fraction upper limit %
<i>XMM-Newton</i>	1	0203910101	2004 Feb.	9.1	11.3 ± 0.5	9.34	6.2
<i>Chandra</i>	2	7287	2006 Jun	9.5	3.21 ± 0.15	4.71	6.5
<i>XMM-Newton</i>	3	0402910101	2006 Aug.	38.3	5.86 ± 0.15	4.91	6.1
<i>XMM-Newton</i>	4	0410581901	2007 Aug.	12.4	0.41 ± 0.01	0.39	6.6
<i>XMM-Newton</i>	5	0560181101	2009 Feb.	48.7	3.70 ± 0.11	3.11	6.5
<i>XMM-Newton</i>	6	0604880101	2010 Feb.	40.4	0.54 ± 0.08	0.52	5.4
<i>Chandra</i>	7	12554	2011 Jun	96.5	0.78 ± 0.03	1.12	5.8

curves for background flares. Only Obsid 0402910101 contained flares and we used the non-flared exposures for our analysis. We checked the filtered event files for photon pile-up by running the task EPATPLOT. No pile-up was apparent in the data. Photon redistribution matrices and ancillary files were created using the SAS tools RMFGEN and ARFGEN, respectively. We rebinned the source spectra using the tool GRPPHA, such that the minimum number of counts per bin of the PN spectra was 25^3 .

2.5 Chandra observations

We analysed two *Chandra* observations of AX J1549.8–5416 performed on Jun 2006 and Jun 2011, respectively (Table 2). We used the CIAO tools (v. 4.5; Fruscione et al. 2006) and standard *Chandra* analysis threads to reduce the data. No background flares were found, so all data were used for further analysis.

The source spectra and light curves were extracted from a circular region with a radius of 20 arcsec centred on the position of AX J1549.8–5416. Background events were obtained from an annular region with an inner (outer) radius of 30 arcsec (60 arcsec). Using the FTOOL GRPPHA, we rebinned the spectra to contain a minimum of 25 photons per bin.

3 ANALYSIS AND RESULTS

3.1 Optical light curves

The top panel of Fig. 2 shows the optical light curve of AX J1549.8–5416 observed by LCOGT in April–June 2015. The source showed two clear outbursts within ~ 40 days, with the two peaks ~ 35 days apart. During the first outburst, the source was observed in *B*, *V*, *R* and *i'*-bands. During the second outburst, the source was observed in *R*-band only, with some higher time resolution (~ 2 minutes) sequences on 2015 June 10. The lower panels of Fig. 2 show two zoom-in plots of the second peak. The source is less variable at

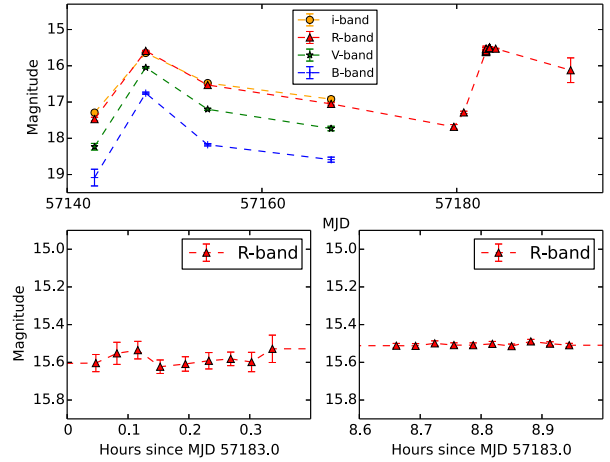


Figure 2. The optical light curve of the source in 2015. The top panel shows the optical light curve of AX J1549.8–5416 in *i'*, *R*, *V* and *B* band with orange, red, green and blue colour, respectively. The bottom panels show two zoom-in plots on the second peak with higher time resolution.

short timescales (minutes) than at longer timescales (~ 10 days).

The general morphology of the outbursts is consistent with a fast rise, exponential decay (FRED; e.g. Chen et al. 1997), with the optical spectrum becoming bluer at higher fluxes. The rise rates between the first and second dates were 2.3, 2.2, 1.9 and 1.6 magnitudes in 5.26 days in *B*, *V*, *R* and *i'*-bands, respectively (0.44, 0.41, 0.36 and 0.31 mag/day). The rise rate of the second outburst was 2.2 mag in 3.3 days in *R*-band (0.65 mag/day), which may suggest the first outburst rise was quicker than measured since the first rise was not well sampled. The decay rates between the second and fourth dates (over 19.0 days) were 0.096, 0.088, 0.077 and 0.067 mag/day in *B*, *V*, *R* and *i'*-bands. The amplitude of the variations are larger at shorter wavelengths, which is expected for an accretion disc described by a simple blackbody that is hotter when it is brighter (this is also the case for low-mass X-ray binaries; see Maitra & Bailyn 2008; Russell et al. 2011).

Serendipitously, our monitoring caught the fast rise of the next outburst, and the short time series coincided almost

³ We found that there are no obvious differences between adding MOS data and using PN spectra only, therefore we only used PN data in this work.

exactly with the peak of the outburst (Fig. 2). On 2015-06-10, the average magnitude was $R = 15.58$ from data taken at 00:02–00:22 UT (9 consecutive images, at a time resolution of 131 sec), and $R = 15.51$ at 08:39–08:58 UT. No intrinsic variability is detected; the magnitudes generally agreed within the errors of each measurement. The conditions were good during the second time series and worse during the first, with mean magnitude measurement errors of 0.048 mag at 00:02–00:22 UT and 0.012 mag at 08:39–08:58 UT. The fractional rms variability (calculated adopting the prescription described in Gandhi et al. 2010) was < 13.7 per cent at 00:02–00:22 UT and < 3.2 per cent at 08:39–08:58 UT (3σ upper limits). To compare this result to observations of other cataclysmic variables, Van de Sande et al. (2015) report fractional rms variability intrinsic to the source in three CVs at a level of 1–5 per cent using data from the *Kepler* satellite (the time resolution was 58.8 sec).

In 2016 we continued monitoring the source in R -band only. We plot the R -band optical light curve of AX J1549.8–5416 with black filled circles in the bottom panel of Fig. 3 between February and May 2016. Starting on Feb 1st (MJD 57419) the source showed three mini-outbursts within ~ 45 days. The time intervals between the three peaks are ~ 15 days. The rising and decaying times are comparable in these three mini-outbursts. The amplitude of the variation is ~ 1 magnitude. Similar anomalous mini-outbursts have also been observed in the DN system SS Cyg (Schreiber et al. 2003).

After the three mini-outbursts the source again went into outburst, with the optical flux increased rapidly (~ 2.6 mag within 5 days, ~ 0.5 mag/day) and then decaying over the next ~ 15 days, both comparable to the two outbursts observed in 2015. This outburst showed a clear FRED morphology and confirmed the DN nature.

In typical DN systems (e.g., SS Cyg, U Gem) the time interval of quiescence is generally longer than the duration of an outburst. Whereas, in the 2015 and 2016 observations of AX J1549.8–5416, the duration at high flux levels is comparable to the time interval at low flux levels, and there appears to be no period of steady flux in quiescence. Instead, the low flux level periods are occupied by mini-outbursts and low level activity.

3.2 Optical spectra

The average optical spectrum (not corrected for intervening Galactic absorption) of AX J1549.8–5416 (Fig. 4) shows the presence of H_α and H_β Balmer lines, and possibly He I $\lambda 6678$, in emission superimposed on an intrinsically blue continuum; the H_β line seems to be embedded in the corresponding absorption feature. All of the detected lines are consistent with being at a redshift of $z = 0$, indicating that this object is within our Galaxy. Fluxes and equivalent widths (EWs) of the two Balmer lines are: $F_{H_\alpha} = (8.5 \pm 1.5) \times 10^{-15}$ erg cm $^{-2}$ s $^{-1}$; $F_{H_\beta} = (3 \pm 1) \times 10^{-15}$ erg cm $^{-2}$ s $^{-1}$; $EW_{H_\alpha} = 9.1 \pm 1.6$ Å; $EW_{H_\beta} = 3 \pm 1$ Å. No He II emission at 4686 Å is detected down to flux and EW 3σ limits of 2×10^{-15} erg cm $^{-2}$ s $^{-1}$ and 2 Å, respectively. These properties do not vary significantly between the two spectra.

Despite the non-optimal signal-to-noise ratio of the optical spectrum, especially in its blue part, its main charac-

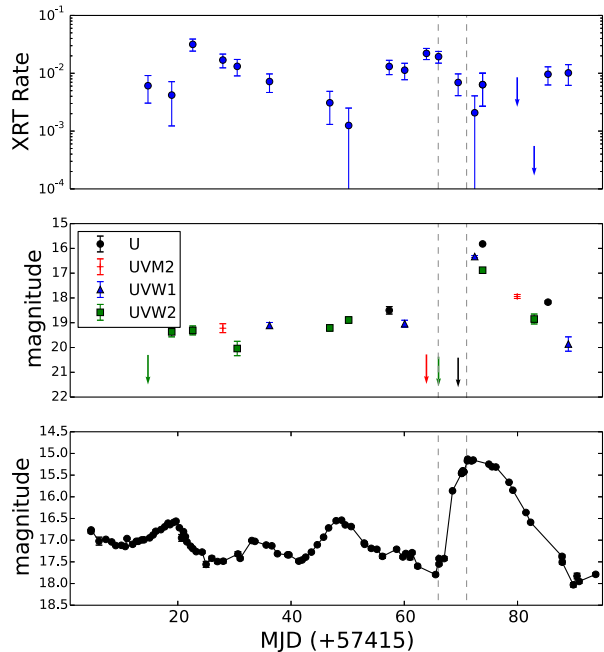


Figure 3. The X-ray, UV and optical light curves of AX J1549.8–5416 are shown in the top, middle and bottom panels, respectively. The rising phase of the outburst is indicated by two vertical dashed lines. The error bars are given at the $1\text{-}\sigma$ level. The observations that only have upper limits are shown by arrows.

teristics depicted above support the identification of NSV 20407 as a CV. Moreover, the lack of apparent He II emission suggests a non-magnetic nature of the accreting WD in this system (see Warner 1995, and references therein for details). Also, the observed H_α/H_β flux ratio (~ 2.8), when compared with the intrinsic one (2.86; Osterbrock 1989) is typical of plasmas in accretion in astrophysical conditions, and points to no substantial reddening in the line of sight towards the object.

3.3 X-ray light curve

Fig. 5 shows the long-term X-ray light curve of AX J1549.8–5416 observed by *Swift*, which indicates its X-ray flux varies by two orders of magnitude. Possibly due to observations being separated by large, irregular amounts of time, we do not find any clear trend in the X-ray light curve.

We converted the *XMM-Newton* and *Chandra* count rates to equivalent *Swift*-XRT count rates using PIMMS in FTOOLS based on the fitted power law indexes shown in Table 4, with results given in Table 2 and shown in Figure 5, respectively. The longer and more sensitive *Chandra* and *XMM-Newton* observations also allowed us to search for significant changes in the X-ray flux on short time-scales. Fig. 6 shows two light curve examples observed by *Chandra* and *XMM-Newton*. At a time resolution of 1000 s, the X-ray intensity varied between 0.001 and 0.015 counts/s, and 0.02 and 0.1 counts/s in *Chandra* and *XMM-Newton* observations, but no clear outbursts are observed.

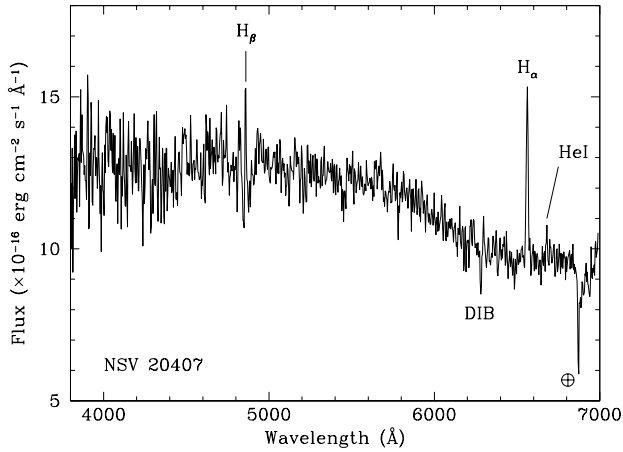


Figure 4. Averaged spectrum of source NSV 20407 as observed at CASLEO on April 14, 2015 (see text for details). The main spectral features are shown. The symbol \oplus indicates atmospheric telluric absorption bands, while the label ‘DIB’ marks the Galactic Diffuse Interstellar Band at 6280 Å.

We also searched for periodic X-ray variability in these observations, which could correspond to the spin or orbital period of the WD. To search for a periodic modulation in the X-ray light curves we created the Leahy power density spectra (PDS) (Leahy et al. 1983) for each observation. We used the pn and ACIS light curves extracted from the source region and binned at the frame readout time from *XMM-Newton* and *Chandra* respectively. We searched for a periodic behaviour of the source in a range between 73.4 ms and 26.8 hour. No significant periodicity (0.5–10 keV) was found in all *XMM-Newton* and *Chandra* observations. We show the $3\text{-}\sigma$ upper limit of the pulsed fraction for each observation in Table 2. The lack of a coherent signal at the WD spin period in the X-ray band suggests that the WD does not possess a strong magnetic field.

3.4 Multi-wavelength observations in 2016

Fig. 3 shows the X-ray/UV/optical observations of AX J1549.8–5416 from February to May 2016. During the phase when the source showed three mini-outbursts, we do not find a clear trend in the UV bands, probably because of the changes between the UVOT filters. At X-ray energies the source shows ~ 2 orders of magnitude variations during these three mini-outbursts. The X-ray flux is highest when the source is in optical quiescence. After the three mini-outbursts, both the optical and UV fluxes decreased and the source went to the quiescent state. The UV emission was not detected before the largest optical outburst.

In the rising phase of the largest optical outburst, the UV emission was still undetected, and the X-ray flux decreased. The UV emission appeared at the time of optical peak, which indicates a UV delay in the rising phase.

Both optical and UV fluxes decreased during the early decaying phase. The X-ray emission was not detectable in this phase. At the end of the outburst the optical and UV fluxes decreased continually, but the X-ray emission recov-

ered. Both the X-ray suppression during the outburst and recovery at the end of the outburst have also been reported in another DN, SS Cyg (Wheatley et al. 2003).

3.5 X-ray – UV and X-ray – optical correlation

Fig. 7 shows the simultaneous UV–X-ray intensity correlation diagrams of AX J1549.8–5416 for the four UVOT filters. In the four UV bands, the X-ray flux is to some extent anti-correlated with the UV flux in this source. In order to describe the correlation quantitatively, we used a constant function and a constant plus a power law function to fit the data in four UVOT filters, respectively. The fitting results are shown in Table 3. The f-test probability suggests that, instead of using a constant function, the data can be better fitted by adding a power law function. The power law indices are all negative and indicate that the UV and X-ray are anti-correlated in the four filters. We also performed a Spearman’s rank correlation coefficient test between X-ray and UV fluxes, and report in Table 3 the value of the Spearman’s rank correlation coefficient and the null hypothesis probability (p-value). The negative correlation coefficient and small p-values again indicate that the UV and X-ray are anti-correlated. We note that the observations with upper limits are not used in the above analysis.

Fig. 8 shows the simultaneous optical–X-ray flux correlation of AX J1549.8–5416 during the 2016 observations. We found that the X-ray and optical flux also show an anti-correlation, which is much clearer at low optical fluxes.

3.6 X-ray Spectral analysis

Due to the low signal-to-noise ratio of this source in an individual *Swift* XRT observation, spectral fitting is not possible, so we used the X-ray colour to study the X-ray spectra with *Swift*. For each observation, we calculated the X-ray hardness. We defined the hardness as the count rate in the 2.0–10.0 keV band divided by the count rate in the 0.3–10.0 keV band. In the upper panel of Fig. 9 we show the hardness-intensity diagram (HID) of the source. The data are rebinned so that each bin has approximately the same counts. As shown in the upper panel of Fig. 9, the X-ray spectrum changes with its flux. Above $\sim 2 \times 10^{-3}$ cnt/s, the X-ray emission is hard, with a constant hardness ratio ~ 0.6 . Below this flux level, its X-ray emission becomes soft. We first fitted these data with a constant function and obtained a χ^2 of 151.2 (dof = 17). We then fitted these data with a power-law model, and got a power-law index of 0.57 ± 0.07 ($1\text{-}\sigma$ error) with a χ^2 of 41.2 (dof = 16). The smaller reduced χ^2 indicates that a power-law fit is better than a constant. We performed a Kolmogorov-Smirnov (K–S) test of our count rates sample against the standard normal distribution. The probability value of K–S test is 0.12, which indicates the source count rates are not consistent with random points around a constant value.

We also measured the X-ray spectrum of the source from four *XMM-Newton* and two *Chandra* X-ray observations (observation 0410581901 was not used due to the low count rate and high background). The spectra were fitted in 0.5–10 keV range with XSPEC (v. 12.8.1 Arnaud 1996). We included the effect of interstellar absorption using WABS assuming cross-sections of Balucinska-Church & McCammon

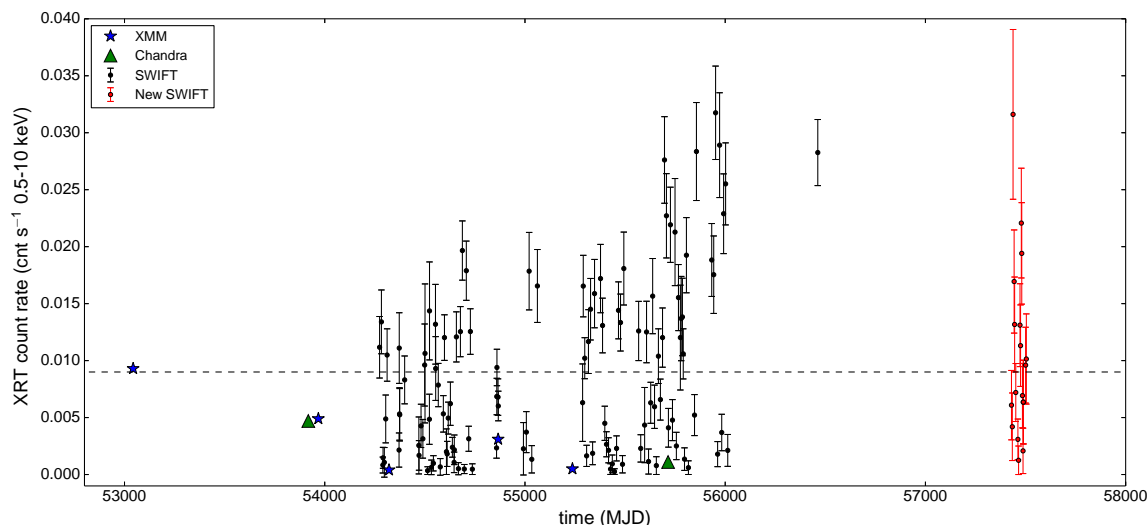


Figure 5. The *Swift*/XRT light curve of AX J1549.8–5416 (one bin per observation) is represented by black and red (2016 observations) filled circles. The error bars are given at the $1\text{-}\sigma$ level. The blue stars indicate the *XMM-Newton* EPIC-pn count rate and the green triangles are the *Chandra* count rate, respectively (converted to the equivalent XRT count rate). The typical spacing between *Swift* observations is $\sim 1 - 2$ weeks in the data before 2016. The horizontal dashed line indicates the 0.009 cnt/s level below which the source is in optical outburst.

Table 3. The fitting parameters of a constant function, a power law with a constant function, correlation coefficient and p-values of Spearman’s rank correlation coefficient test for the UV – X-ray correlation.

data	constant χ^2 (dof)	Γ	power law + constant χ^2 (dof)	f-test probably	correlation coefficient	p-value (%)
U	159.7(15)	-2.2 ± 0.8	89.5(13)	2.3×10^{-2}	-0.52	3.87
UVM2	217(14)	-3.8 ± 1.1	58.3(12)	3.7×10^{-4}	-0.54	3.59
UVW1	156(15)	-0.6 ± 0.2	29.4(13)	1.9×10^{-5}	-0.76	0.03
UVW2	120(17)	-0.2 ± 0.1	65.5(15)	3.9×10^{-3}	-0.74	2.03

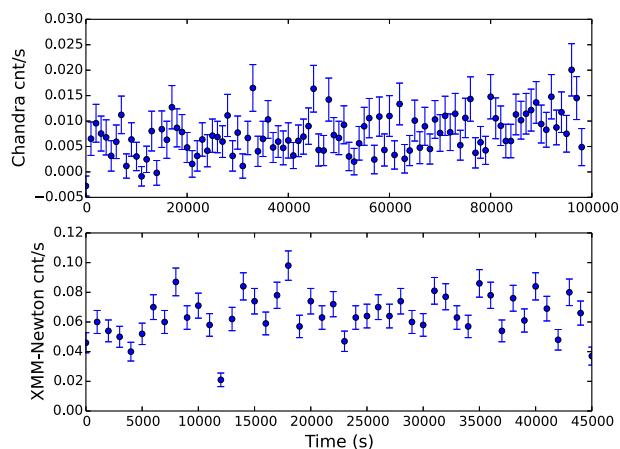


Figure 6. Top panel: the light curve of AX J1549.8–5416 observed by *Chandra* in Obsid 12554 in Jun 2011; bottom panel: the light curve of the source observed by *XMM-Newton* in Obsid 0402910101 in Aug 2006. Both light curves are binned at 1000s.

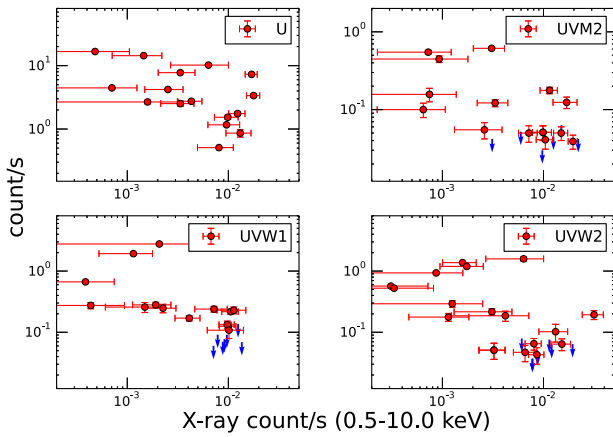
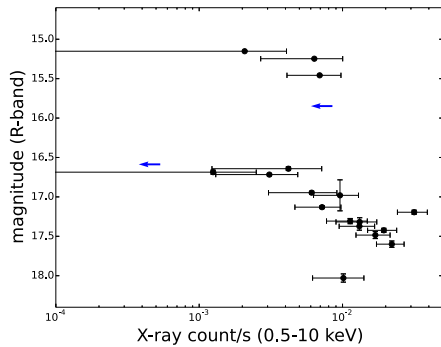
(1992) and solar abundances from Anders & Grevesse (1989), and we let N_{H} , the column density along the line of sight, vary during the fitting.

In order to understand the source spectral shape at different flux levels, we first used a power-law model to fit all spectra. The continuum spectra can be well fitted by a power-law model except some residuals around 6.7 keV, which may come from Iron lines. The N_{H} shows comparable values, $\sim (4 - 5) \times 10^{21}\text{ cm}^{-2}$, in all spectra. The fitted power-law parameters are shown in Table 4. The spectrum photon index is larger when the source is at a low X-ray flux level than at a high X-ray flux level. This is consistent with the XRT X-ray hardness analysis above. There is no need to include a soft component below 1 keV in all spectral fits.

As argued above, the optical light curves and spectra indicate the source is a DN. The simple model which is often used in DNe consists of a single-temperature optically thin thermal plasma model (MEKAL in XSPEC, e.g. Mewe et al. 1985). This model has been successfully used in ~ 30 spectra of dwarf novae (Baskill et al. 2005) observed with ASCA. We also used this model to fit all our X-ray spectra separately. Because the abundance derived by MEKAL is consistent with solar abundance within uncertainty, we then fixed

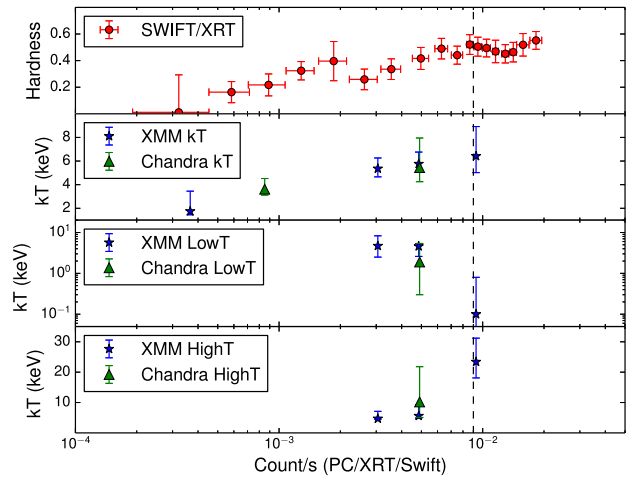
Table 4. Fit statistics and parameters of the spectra models POWERLAW and MEKAL applied to the six X-ray spectrum of AX J1549.8–5416. Error bars are given in 90% confidence levels.

ObsID	N_{H} (PL) 10^{22} cm^2	Γ_{PL}	reduced χ^2 (PL)	N_{H} (MK) 10^{22} cm^2	kT keV	norm $\times 10^{-4}$	reduced χ^2 (MK)
0203910101	$0.38^{+0.11}_{-0.10}$	$1.75^{+0.22}_{-0.21}$	1.01	$0.31^{+0.08}_{-0.07}$	$6.81^{+3.41}_{-1.84}$	$7.4^{+0.5}_{-0.7}$	0.91
7287	$0.36^{+0.27}_{-0.23}$	$1.85^{+0.42}_{-0.38}$	0.94	$0.33^{+0.21}_{-0.18}$	$5.12^{+5.62}_{-1.69}$	$3.4^{+0.7}_{-0.5}$	0.87
0402910101	$0.50^{+0.07}_{-0.06}$	$2.04^{+0.14}_{-0.13}$	1.71	$0.35^{+0.05}_{-0.05}$	$5.45^{+1.00}_{-0.79}$	$3.5^{+0.2}_{-0.2}$	1.21
0560181101	$0.49^{+0.07}_{-0.06}$	$2.05^{+0.16}_{-0.15}$	1.37	$0.36^{+0.05}_{-0.04}$	$5.02^{+0.96}_{-0.75}$	$2.9^{+0.2}_{-0.2}$	1.32
0604880101	$0.52^{+0.33}_{-0.26}$	$3.49^{+1.36}_{-0.91}$	2.21	$0.04^{+0.15}_{-0.04}$	$2.67^{+1.22}_{-0.71}$	$0.35^{+0.10}_{-0.07}$	1.57
12554	$0.45^{+0.34}_{-0.21}$	$2.45^{+0.21}_{-0.19}$	1.21	$0.05^{+0.07}_{-0.04}$	$6.08^{+3.01}_{-1.45}$	$0.77^{+0.07}_{-0.07}$	0.91

**Figure 7.** Simultaneous UV–X-ray intensity diagrams for four UVOT filters. The error bars are given at the $1\text{-}\sigma$ level. The blue arrows indicate UV upper limits.**Figure 8.** Simultaneous X-ray–optical flux correlation of AX J1549.8–5416. The error bars are given at the $1\text{-}\sigma$ level. The blue arrows indicate X-ray the upper limits.

the abundance to 1 in our analysis. The fitted parameters are shown in Table 4. With the same degree of freedom and smaller χ^2 in each observation, the MEKAL model gives a better fit than the power-law model.

From Table 4 the N_{H} shows a similar value at different X-ray flux levels. In order to better understand the evolution of the thermal plasma temperature at different flux levels, we fitted the six spectra simultaneously with linked N_{H} .

**Figure 9.** Top panel: the hardness-intensity diagram of AX J1549.8–5416 observed by *Swift*. Second panel: the plasma temperature (in MEKAL) as a function of X-ray intensity. Third and fourth panels: the kT_{Low} and kT_{High} (in MKCFLOW) as a function of X-ray intensity. We converted the *XMM-Newton* and *Chandra* intensity to equivalent *Swift* intensity. The vertical dashed line indicates the 0.009 cnt/s level.

The N_{H} value from the simultaneous fitting is $(0.33 \pm 0.03) \times 10^{22} \text{ cm}^2$, which is comparable with values from individual spectrum fits in Table 5. Fig. 10 shows the X-ray spectrum of each observation (four *XMM-Newton* and two *Chandra*) overlaid with best-fitting MEKAL model. The best-fitting reduced χ^2 is 1.29 with 296 degrees of freedom. The iron line is clearly detected in bf the four observations which have higher X-ray flux.

It is clear from Table 5 that the temperature of the thermal plasma is higher when the source has higher X-ray flux. The second panel of Fig.-9 shows the plasma temperature as a function of X-ray intensity. When the source is in the high intensity state, the X-ray spectra show comparable plasma temperature at ~ 6 keV. When the source evolves to low intensity levels, the plasma temperature decreases significantly to ~ 1.5 keV. We find that the normalization of MEKAL also decreases as the X-ray flux decreases.

As discussed in Section 3.5, the large variations in both X-ray and UV bands and the anti-correlation between X-ray and UV emission suggest that the source is a DN

Table 5. Fit results for the MEKAL model applied to six combined X-ray spectra of AX J1549.8–5416. The absorbed 0.5–10 keV flux are also reported. Error bars are given at the 90% confidence level. The N_{H} was linked across the spectra and the value is $0.33 \pm 0.03 \times 10^{22} \text{ cm}^2$.

ObsID	kT keV	Normalization (MK) 10^{-4}	flux (0.5–10 keV) $10^{-13} \text{ erg/cm}^2/\text{s}$
0203910101	$6.42^{+2.53}_{-1.43}$	$7.56^{+0.56}_{-0.55}$	$11.76^{+1.23}_{-2.05}$
7287	$5.15^{+2.52}_{-1.23}$	$3.47^{+0.35}_{-0.34}$	$5.01^{+0.71}_{-0.51}$
0402910101	$5.76^{+1.03}_{-0.73}$	$3.41^{+0.17}_{-0.16}$	$5.13^{+0.23}_{-0.21}$
0560181101	$5.36^{+0.98}_{-0.78}$	$2.84^{+0.15}_{-0.15}$	$4.15^{+0.19}_{-0.41}$
0604880101	$1.75^{+0.72}_{-0.38}$	$0.43^{+0.13}_{-0.09}$	$0.43^{+0.11}_{-0.12}$
12554	$3.62^{+0.93}_{-0.56}$	$0.96^{+0.07}_{-0.07}$	$1.18^{+0.05}_{-0.09}$

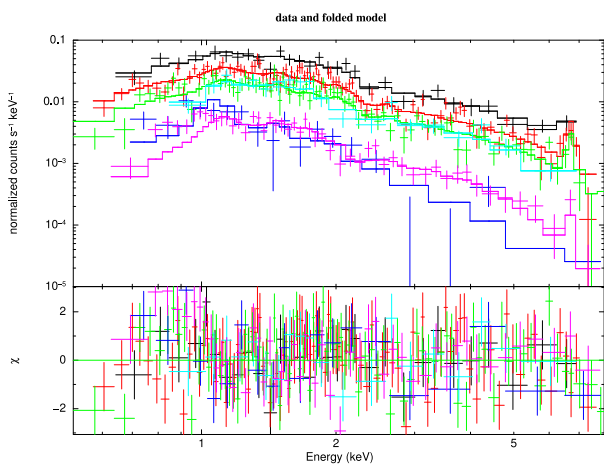


Figure 10. The *XMM-Newton* PN, and *Chandra* ACIS spectra of AX J1549.8–5416 in the 0.5–10.0 keV energy band. The spectrum was fitted with a single-temperature thin thermal plasma model. The six spectra are represented by six different colour curves in the upper panel. The lower panel shows the residuals to the best-fitting models. The observations 1, 2, 3, 5, 6 and 7 (in Table-2) are shown in black, light blue, red, green, purple and blue, respectively.

(Wheatley et al. 2003; Collins & Wheatley 2010; Britt et al. 2015). We therefore also used an isobaric cooling flow model, MKCFLOW, to fit the X-ray emission from the source (Mushotzky & Szymkowiak 1988). This model is often used to describe the X-ray spectrum of DNe in optical quiescence (Pandel et al. 2005; Mukai et al. 2009; Byckling et al. 2010). Unlike the single temperature plasma model, the cooling flow model is assumed to consist of a range of temperatures. In the model, the temperature varies from the hot shock temperature (kT_{High}) to the temperature of the optically thin cooling matter (kT_{Low}) on the WD surface. Thus, cooling flow spectral models should represent a more physically correct picture of the cooling plasma.

Due to the low X-ray count rate and the numerous parameters in MKCFLOW, we only used this model to fit the spectrum obtained from observations with > 300 counts. In the following analysis we only used observations 1, 2, 4 and 5 (see Table 2). The parameters are shown in Table 6. We note that, as the X-ray flux decreases, the normalization (accretion rate) increases, kT_{Low} increases and kT_{High} decreases. The temperature separation ($kT_{\text{High}} - kT_{\text{Low}}$) decreases when the X-ray flux decreases.

Further-more, we first linked the kT_{High} to the same value in all four observations and then let it be free in observation 1. The χ^2 reduced from 278.15 (227 dof) to 268.21 (226 dof). This indicates that the source in observations 2, 4 and 5 has a different X-ray spectrum than that in observation 1.

4 DISCUSSION

4.1 AX J1549.8–5416 is a DN

We have analysed new optical light curves and spectra of the CV AX J1549.8–5416. We detected three outbursts and three mini-outbursts in the 2015 and 2016 optical light curve. We also detected H_{α} and H_{β} lines in the optical spectrum. Both the fast rise and exponential decay optical outbursts and the lack of apparent He II emission lines in the optical spectra suggest that AX J1549.8–5416 is a non-magnetic CV. This is not consistent with the MCV classification reported by Lin et al. (2014).

We then analysed all available archival data from *Swift*, *XMM-Newton* and *Chandra*, and find that the source is also highly variable at UV and X-ray wavelengths. We find that the X-ray intensity increases with X-ray hardness. We also find an anti-correlation between X-ray and UV flux in this source. The high-resolution X-ray spectra of *XMM-Newton* and *Chandra* can be well described either by a single temperature thermal plasma model or by an isobaric cooling flow model when its X-ray flux is high. The behavior of the X-ray and UV evolution in this system is very similar to other DNe (e.g. SS Cyg, SU UMa, Wheatley et al. 2003; McGowan et al. 2004; K rding et al. 2008), and further confirms that AX J1549.8–5416 is a DN.

From X-ray timing analysis of this system we did not find a significant periodic signal from all *XMM-Newton* and *Chandra* observations, which is in common with other DNe. Baskill et al. (2005) analyzed 34 non-MCVs (20 are DNe) observed by *ASCA* and found that most of the sources do not show periodic modulation of their X-ray flux.

4.2 UV delay and X-ray suppression during the outburst in AX J1549.8–5416

We studied the behaviour of the optical, UV and X-ray emission during the outburst to help us to understand the movement of material through the accretion disc. We observed

Table 6. Fit parameters of the spectral models MKCFLOW applied to the four X-ray spectra of AX J1549.8–5416. Error bars are given at the 90% confidence level.

ObsID	kT _{Low} keV	kT _{High} keV	Normalization (MK) 10 ⁻¹¹ M _⊙ /yr	flux (0.5–10 keV) 10 ⁻¹³ erg/cm ² /s
0203910101	0.1 ^{+1.4} _{-0.08}	23.5 ^{+7.8} _{-5.3}	10.7 ^{+3.4} _{-3.3}	11.2 ^{+1.5} _{-3.2}
7287	1.9 ^{+4.8} _{-1.8}	10.5 ^{+20.5} _{-6.1}	10.8 ^{+290.7} _{-7.4}	4.8 ^{+0.2} _{-1.2}
0402910101	4.1 ^{+0.6} _{-2.6}	6.3 ^{+6.2} _{-1.5}	65.6 ⁺²²³ _{-45.4}	4.9 ^{+0.2} _{-0.2}
0560181101	3.8 ^{+1.4} _{-2.1}	5.8 ^{+7.6} _{-1.5}	120.5 ^{+354.8} _{-95.4}	4.0 ^{+0.1} _{-0.4}

AX J1549.8–5416 in 2016 with a dedicated optical, UV and X-ray campaign and detected three mini-outbursts and one normal outburst. We find that the UV emission is clearly delayed with respect to the optical emission during the rising phase of the outburst (see Fig. 3). The first optical rise occurred between MJD 57482.04 and 57483.52. The UV emission was still not detectable on MJD 57484.51, so the UV delay must be longer than 1.0 day. The UV became bright on MJD 574487.44, which indicates the UV delay must be less than 5.4 days. Due to the long separation between *Swift* observations, we can therefore only constrain the delay time to be $\sim 1.0 - 5.4$ day, The UV delay during the rising phase of DN outbursts has already been reported (e.g., VW Hydri, U Gem and SS Cyg, Cannizzo 2001; Wheatley et al. 2003). Wheatley et al. (2003) find that in DN SS Cyg the UV emission delays the optical emission by $\sim 1.5 - 2$ days during the outburst rise, comparable to what we infer for AX J1549.8–5416.

Wheatley et al. (2003) find that in SS Cyg the X-ray flux first rises fast and then drops immediately during the optical outburst rising phase (see also Russell et al. 2016). During the rise of the outburst in AX J1549.8–5416, we also detect X-ray emission significantly lower than that observed before the outburst (quiescence). However, we do not find a spike in X-ray during the outburst rise of AX J1549.8–5416. Since the separation of our *Swift* observations is ~ 3 days and the duration of the X-ray spike in SS Cyg is ~ 1 day, it is likely that we missed the spike shape variation in our X-ray observations. Similar to SS Cyg we also find the suppression and recovery of the X-ray emission during the middle and the end of the optical outburst, respectively.

Outbursts of DNe are generally interpreted as a sudden brightening of the optically thick accretion disc due to an increased accretion rate (e.g., Osaki 1996; Lasota 2001). The UV delay time has been used to measure the heating wave propagation time (Cannizzo 2001; Wheatley et al. 2003; Schreiber et al. 2003). Unfortunately our optical/UV data are not sufficient to allow us to estimate the beginning and timescale of the propagation of the heating wave.

The suppression of the X-ray emission during an outburst has been interpreted as the boundary layer becoming optically thick to its own radiation. At the end of the outburst the boundary layer switches back to optically thin, the inner disc truncates and emits in the X-ray band (Cannizzo 2001; Wheatley et al. 2003).

4.3 Mini-outbursts

AX J1549.8–5416 showed three mini-outbursts in the 2016 optical observations. Similar anomalous outbursts have also been observed in SS Cyg (Schreiber et al. 2003). These kind of mini-outbursts cannot be reproduced by the standard disc instability model (DIM). Schreiber et al. (2003) managed to reproduce the mini-outbursts by modifying the DIM. The simulated mini-outburst light curve shows a short rise time and a sharp peak. However, the observed mini-outbursts show rise times (~ 9 days) and similarly slow decays. In their simulations, they assume the disc extends down to the surface of the WD (no truncation) and heating of the outer disc and tidal dissipation are completely neglected.

4.4 X-ray spectra of AX J1549.8–5416 in outburst and quiescence

The X-ray spectra of DNe changes dramatically between optical quiescence and outburst. In quiescence, X-ray spectra are normally described by multi-temperature optically thin thermal models, such as observed from cooling flows. In outburst, the emission is instead described by optically thick emission in the EUV band, with characteristic temperatures around 10 eV. The X-ray spectrum is softer and the temperature is lower than that in optical quiescence (e.g., Baskill et al. 2005; Collins & Wheatley 2010). In Fig. 9, we show that the plasma temperature decreases as the X-ray flux decreases (optical flux increases). The evolution of X-ray spectra of AX J1549.8–5416 can be well interpreted by the DN hypothesis.

We also used an isobaric cooling flow model to re-analyse the four observations (Obs 1, 2, 3 and 5) when the source had higher X-ray flux. This model is often used to describe the quiescent X-ray spectrum of DNe (Pandel et al. 2005; Mukai et al. 2009; Byckling et al. 2010). The four spectra are well fitted by the cooling flow model. As the X-ray flux decreases, the temperature separation ($kT_{High} - kT_{Low}$) decreases as well, which indicates the X-ray emission became optically thick. This is also consistent with the DN hypothesis (Kuulkers et al. 2006; Patterson 2011; Balman 2012).

Ishida et al. (2009) analysed data from *Suzaku* observations of the DN SS Cyg in quiescence and outburst. They found the maximum temperature of the plasma is ~ 20 keV and ~ 6 keV in quiescence and outburst, respectively. McGowan et al. (2004) also found that the plasma temperature is ~ 20 keV when SS Cyg is in quiescence. From Table 6 we find that only Obs 1 has a maximum plasma temperature higher than 20 keV. This suggests that only Obs 1

was observed in quiescence if we assume AX J1549.8–5416 and SS Cyg have comparable maximum plasma temperature in quiescence and outburst. The maximum temperature of the plasma in quiescence is significantly higher than that in outburst in AX J1549.8–5416.

4.5 Duty cycle

In DNe the X-ray flux is always suppressed during optical outbursts and then shows a general anti-correlation with optical flux (Wheatley et al. 2003; McGowan et al. 2004). Since we have a large number of XRT observations, instead of using optical observations, we can use the X-ray data to roughly estimate the duty cycle of AX J1549.8–5416. We define the outburst state when the X-ray intensity is lower than 0.009 cnt/s (see Fig. 5 and 9). This threshold is lower than the equivalent XRT intensity of Obs 1 which was believed to be in quiescence. The calculated duty cycle of AX J1549.8–5416 is $\sim 51\%$. Due to the random and long separation of the XRT observations, the estimated duty cycle may have a large uncertainty. We used highest 10% of the X-ray intensities (~ 0.003 cnt/s) to estimate the uncertainty of the threshold. With the threshold in the range of 0.006 – 0.012 cnt/s, we estimate a duty cycle in the range of 35% – 60%.

The estimated $\sim 50\%$ duty cycle indicates that this source is a very active DN with comparable quiescence and outburst time. Fig. 3 shows that AX J1549.8–5416 is very active in our new optical observations and also shows comparable quiescence and outburst time. The new optical light curves support the estimated high duty cycle in AX J1549.8–5416.

Britt et al. (2015) recently measured the duty cycles for an existing sample of well-observed, nearby DNe and derived a quantitative empirical relation between the duty cycle of DNe outbursts and the X-ray luminosity of the system in quiescence. If we assume this relationship also applies to AX J1549.8–5416, the estimated $\sim 50\%$ duty cycle suggests the X-ray luminosity of this system should be larger than 10^{32} erg/s in quiescence. This suggests that AX J1549.8–5416 might belong to a class of DNe with both high average mass transfer rate in outburst and high instantaneous accretion rate in quiescence. Assuming the X-ray flux of this source in quiescence is larger than $\sim 1.2 \times 10^{-13}$ erg/cm²/s (see Table 5), we could estimate the distance to AX J1549.8–5416 to be $\lesssim 1.0$ kpc. We note that neither the duty cycle nor the X-ray luminosity in quiescence are able to entirely reliably trace the mass accretion rate of the system (Britt et al. 2015).

5 CONCLUSIONS

In this paper we analyse new optical/UV/X-ray light curves and spectra of the peculiar CV AX J1549.8–5416. Both the FRED optical outbursts and the lack of apparent He II emission lines in the optical spectra suggest that AX J1549.8–5416 is a typical DN. We present multi-wavelength (optical/UV/X-ray) observations of DN AX J1549.8–5416 throughout three mini-outbursts and one normal outburst. We find the UV emission delays the optical emission by 1.0 – 5.4 days during the rising phase of the outburst. The

X-ray emission shows suppression during the outburst peak and recovery during the end of the outburst.

We also analyse archival *Swift*, *Chandra* and *XMM-Newton* observations of AX J1549.8–5416. We find an approximately anti-correlation between X-ray and UV flux. The high-resolution X-ray spectra from *XMM-Newton* and *Chandra* can be well described either by a single temperature thermal plasma model or by an isobaric cooling flow model when its X-ray flux is high. We find the maximum temperature of the plasma in quiescence is significant higher than that in outburst in AX J1549.8–5416. Our estimated high duty cycle suggests that the X-ray luminosity of this source should be larger than 10^{32} erg/s in quiescence.

ACKNOWLEDGEMENTS

This work makes use of optical observations from the Las Cumbres Observatory Global Telescope Network, and has made use of the LCOGT Archive, which is operated by the California Institute of Technology, under contract with the Las Cumbres Observatory. The X-ray data are obtained from the High Energy Astrophysics Science Archive Research Center (HEASARC), provided by NASA’s Goddard Space Flight Center and NASA’s Astrophysics Data System Bibliographic Services. We thank Mallory Roberts for useful comments and discussions. We thank B. Sbarufatti, K. L. Page and D. Malesani for approving our *Swift* ToO (target ID 42706) and the *Swift* Science Operations Team for performing the observations.

REFERENCES

- Anders E., Grevesse N., 1989, *Geochim. Cosmochim. Acta*, 53, 197
- Arnaud K. A., 1996, in G. H. Jacoby & J. Barnes ed., *Astronomical Data Analysis Software and Systems V* Vol. 101 of *Astronomical Society of the Pacific Conference Series*, *XSPEC: The First Ten Years*. p. 17
- Balman S., 2012, *MnSAI*, 83, 585
- Balucinska-Church M., McCammon D., 1992, *ApJ*, 400, 699
- Baskill D. S., Wheatley P. J., Osborne J. P., 2005, *MNRAS*, 357, 626
- Blackburn J. K., 1995, in Shaw R. A., Payne H. E., Hayes J. J. E., eds, *Astronomical Data Analysis Software and Systems IV* Vol. 77 of *Astronomical Society of the Pacific Conference Series*, *FTOOLS: A FITS Data Processing and Analysis Software Package*. p. 367
- Britt C. T., Maccarone T., Pretorius M. L., Hynes R. I., Jonker P. G., Torres M. A. P., Knigge C., Johnson C. O., Heinke C. B., Steeghs D., Greiss S., Nelemans G., 2015, *MNRAS*, 448, 3455
- Brown P. J., Holland S. T., Immler S., Milne P., Roming P. W. A., Gehrels N., Nousek J., Panagia N., Still M., Vanden Berk D., 2009, *AJ*, 137, 4517
- Burrows D. N., Hill J. E., Nousek J. A., Kennea J. A., Wells A., Osborne J. P., Abbey A. F., Beardmore A., Mukerjee K., Short A. D. T., Chincarini G., Campana S., Citterio O., Moretti A., Pagani C., 2005, *Space Sci. Rev.*, 120, 165

- Byckling K., Mukai K., Thorstensen J. R., Osborne J. P., 2010, *MNRAS*, 408, 2298
- Cannizzo J. K., 2001, *ApJ*, 556, 847
- Chen W., Shrader C. R., Livio M., 1997, *ApJ*, 491, 312
- Collins D. J., Wheatley P. J., 2010, *MNRAS*, 402, 1816
- Evans P. A., Beardmore A. P., Page K. L., Osborne J. P., O'Brien P. T., Willingale R., Starling R. L. C., Burrows D. N., Godet O., Vetere L., Racusin J., Goad M. R., Wiersema K. a., 2009, *MNRAS*, 397, 1177
- Ezuka H., Ishida M., 1999, *ApJS*, 120, 277
- Fruscione A., McDowell J. C., Allen G. E., Brickhouse N. S., Burke D. J., Davis J. E., Durham N., 2006, 6270, 1
- Gandhi P., Dhillon V. S., Durant M., Fabian A. C., Kubota A., Makishima K., Malzac J., Marsh T. R., Miller J. M., Shahbaz T., Spruit H. C., Casella P., 2010, *MNRAS*, 407, 2166
- Henden A. A., Levine S., Terrell D., Welch D. L., 2015, in *American Astronomical Society Meeting Abstracts Vol. 225 of American Astronomical Society Meeting Abstracts, APASS - The Latest Data Release*. p. 336.16
- Horne K., 1986, *PASP*, 98, 609
- Ishida M., Okada S., Hayashi T., Nakamura R., Terada Y., Mukai K., Hamaguchi K., 2009, *PASJ*, 61, S77
- Jordi K., Grebel E. K., Ammon K., 2006, *A&A*, 460, 339
- Körding E., Rupen M., Knigge C., Fender R., Dhawan V., Templeton M., Muxlow T., 2008, *Science*, 320, 1318
- Kuulkers E., Norton A., Schwobe A., Warner B., 2006, *X-rays from cataclysmic variables*. pp 421–460
- Lasota J., 2001, *New Astronomy Review*, 45, 449
- Leahy D. A., Darbro W., Elsner R. F., Weisskopf M. C., Kahn S., Sutherland P. G., Grindlay J. E., 1983, *ApJ*, 266, 160
- Lewis F., Russell D. M., Fender R. P., Roche P., Clark J. S., 2008, in *Proc. VII Microquasar Workshop: Microquasars and Beyond, Proceedings of Science. SISSA, Trieste, PoS(MQW7)069*
- Lin D., Webb N. A., Barret D., 2014, *ApJ*, 780, 39
- Maitra D., Bailyn C. D., 2008, *ApJ*, 688, 537
- McGowan K. E., Priedhorsky W. C., Trudolyubov S. P., 2004, *ApJ*, 601, 1100
- Mewe R., Gronenschild E. H. B. M., van den Oord G. H. J., 1985, *A&AS*, 62, 197
- Meyer F., Meyer-Hofmeister E., 1981, *A&A*, 104, L10
- Mukai K., Zietsman E., Still M., 2009, *ApJ*, 707, 652
- Mushotzky R. F., Szymkowiak A. E., 1988, in Fabian A. C., ed., *NATO Advanced Science Institutes (ASI) Series C Vol. 229 of NATO Advanced Science Institutes (ASI) Series C, Einstein Observatory solid state detector observations of cooling flows in clusters of galaxies*. pp 53–62
- Osaki Y., 1996, *PASP*, 108, 39
- Osterbrock D. E., 1989, *Astrophysics of gaseous nebulae and active galactic nuclei*
- Pandel D., Córdova F. A., Howell S. B., 2003, *MNRAS*, 346, 1231
- Pandel D., Córdova F. A., Mason K. O., Priedhorsky W. C., 2005, *ApJ*, 626, 396
- Patterson J., 2011, *MNRAS*, 411, 2695
- Russell D. M., Maitra D., Dunn R. J. H., Fender R. P., 2011, *MNRAS*, 416, 2311
- Russell T. D., Miller-Jones J. C. A., Sivakoff G. R., Altamirano D., O'Brien T. J., Page K. L., Templeton M. R., Koerding E. G., Knigge C., Rupen M. P., Fender R. P., Heinz S., Maitra D., 2016, *MNRAS*, 460, 3720
- Saitou K., Tsujimoto M., Ebisawa K., Ishida M., 2012, *PASJ*, 64, 88
- Samus N. N., Durlevich O. V., et al. 2009, *VizieR Online Data Catalog*, 1, 2025
- Schreiber M. R., Hameury J.-M., Lasota J.-P., 2003, *A&A*, 410, 239
- Singh K. P., 2013, in Das S., Nandi A., Chattopadhyay I., eds, *Astronomical Society of India Conference Series Vol. 8 of Astronomical Society of India Conference Series, X-ray emission from magnetic cataclysmic variables*. pp 115–122
- Sugizaki M., Mitsuda K., Kaneda H., Matsuzaki K., Yamauchi S., Koyama K., 2001, *ApJS*, 134, 77
- Tody D., 1993, in Hanisch R. J., Brissenden R. J. V., Barnes J., eds, *Astronomical Data Analysis Software and Systems II Vol. 52 of Astronomical Society of the Pacific Conference Series, IRAF in the Nineties*. p. 173
- Van de Sande M., Scaringi S., Knigge C., 2015, *MNRAS*, 448, 2430
- Warner B., 1995, *Cambridge Astrophysics Series*, 28
- Wheatley P. J., Mauche C. W., Mattei J. A., 2003, *MNRAS*, 345, 49

APPENDIX A: LOG OF LCOGT 2015 AND 2016 OBSERVATIONS.

We observed the field of AX J1549.8–5416 with LCOGT suite of robotic 1-m telescopes in 2015 and 2016. Some data in 2016 were taken with the 2-m Faulkes Telescope South (FTS). All 1-m telescopes are equipped with a camera with pixel scale $0.467 \text{ arcsec pixel}^{-1}$; this is $0.304 \text{ arcsec pixel}^{-1}$ for the 2-m data. We adopt a 2.8 arcsec aperture for the 1-m data and 1.8 arcsec aperture for the 2-m data, to match the average seeing differences between the 1-m and 2-m data. The observation logs are provided in Table A1 and the telescopes are:

- 1m0-03 = Siding Spring, Australia
- 1m0-05 = Cerro Tololo, Chile
- 1m0-10 = SAAO, South Africa
- 1m0-11 = Siding Spring, Australia
- 1m0-12 = SAAO, South Africa
- 1m0-13 = SAAO, South Africa
- FTS = 2m telescope at Siding Spring, Australia

Table A1. Log of LCOGT 2015 and 2016 observations.

Date UT	MJD	magnitude (R)	Telescope	Filters	Exposure times (s)
2015-04-30	57142.81028	17.471 ± 0.051	1m0-10	B, V, R, i'	100,100,100,100
2015-05-06	57148.06933	15.589 ± 0.014	1m0-05	B, V, R, i'	200,100,100,100
2015-05-12	57154.42698	16.530 ± 0.016	1m0-11	B, V, R, i'	200,100,100,100
2015-05-25	57167.10270	17.051 ± 0.034	1m0-10	B, V, R, i'	200,100,100,100
2015-06-06	57179.70814	17.684 ± 0.062	1m0-12	R	100
2015-06-07	57180.72358	17.285 ± 0.033	1m0-13	R	100
2015-06-10	57183.00197	15.604 ± 0.046	1m0-10	R	100
2015-06-10	57183.00341	15.552 ± 0.059	1m0-10	R	100
2015-06-10	57183.00483	15.535 ± 0.047	1m0-10	R	100
2015-06-10	57183.00637	15.623 ± 0.036	1m0-10	R	100
2015-06-10	57183.00809	15.609 ± 0.038	1m0-10	R	100
2015-06-10	57183.00970	15.592 ± 0.043	1m0-10	R	100
2015-06-10	57183.01119	15.582 ± 0.036	1m0-10	R	100
2015-06-10	57183.01262	15.598 ± 0.051	1m0-10	R	100
2015-06-10	57183.01405	15.528 ± 0.073	1m0-10	R	100
2015-06-10	57183.36087	15.512 ± 0.012	1m0-03	R	100
2015-06-10	57183.36218	15.513 ± 0.012	1m0-03	R	100
2015-06-10	57183.36349	15.499 ± 0.013	1m0-03	R	100
2015-06-10	57183.36481	15.509 ± 0.012	1m0-03	R	100
2015-06-10	57183.36612	15.509 ± 0.012	1m0-03	R	100
2015-06-10	57183.36744	15.502 ± 0.013	1m0-03	R	100
2015-06-10	57183.36875	15.514 ± 0.011	1m0-03	R	100
2015-06-10	57183.37007	15.489 ± 0.011	1m0-03	R	100
2015-06-10	57183.37138	15.501 ± 0.010	1m0-03	R	100
2015-06-10	57183.37270	15.509 ± 0.010	1m0-03	R	100
2015-06-10	57183.99798	15.527 ± 0.010	1m0-05	R	100
2016-02-01	57419.66520	16.796 ± 0.040	1m0-03	R	200
2016-02-01	57419.69488	16.764 ± 0.017	1m0-03	R	200
2016-02-03	57421.08700	17.022 ± 0.092	1m0-10	R	200
2016-02-04	57422.29909	16.981 ± 0.017	1m0-05	R	200
2016-02-05	57423.33328	17.041 ± 0.025	1m0-05	R	200
2016-02-06	57424.03382	17.124 ± 0.022	1m0-13	R	200
2016-02-07	57425.03107	17.118 ± 0.022	1m0-13	R	200
2016-02-07	57425.72135	17.146 ± 0.024	FTS	R	120
2016-02-08	57426.02834	16.963 ± 0.019	1m0-10	R	200
2016-02-09	57427.02551	17.095 ± 0.038	1m0-13	R	200
2016-02-09	57427.68389	17.026 ± 0.033	FTS	R	120
2016-02-10	57428.02394	17.026 ± 0.021	1m0-13	R	200
2016-02-10	57428.63314	16.994 ± 0.020	FTS	R	120
2016-02-11	57429.04155	16.992 ± 0.019	1m0-13	R	200
2016-02-12	57430.02881	16.947 ± 0.019	1m0-10	R	200
2016-02-12	57430.62836	16.880 ± 0.019	FTS	R	120
2016-02-13	57431.11716	16.795 ± 0.034	1m0-13	R	200
2016-02-14	57432.01188	16.757 ± 0.017	1m0-13	R	200
2016-02-14	57432.69475	16.691 ± 0.016	FTS	R	120
2016-02-15	57433.26795	16.607 ± 0.013	1m0-05	R	200
2016-02-15	57433.62776	16.642 ± 0.023	FTS	R	120
2016-02-16	57434.26027	16.590 ± 0.013	1m0-05	R	200
2016-02-16	57434.68099	16.562 ± 0.022	FTS	R	120
2016-02-17	57435.27446	16.713 ± 0.014	1m0-05	R	200
2016-02-17	57435.67131	16.947 ± 0.079	FTS	R	120
2016-02-18	57436.01093	16.803 ± 0.016	1m0-10	R	200
2016-02-18	57436.34304	16.918 ± 0.015	1m0-05	R	200
2016-02-18	57436.61226	17.040 ± 0.025	FTS	R	120
2016-02-19	57437.25208	17.138 ± 0.024	1m0-05	R	200
2016-02-19	57437.65759	17.195 ± 0.026	FTS	R	120
2016-02-20	57438.25358	17.264 ± 0.030	1m0-05	R	200
2016-02-21	57439.29170	17.274 ± 0.032	1m0-05	R	200
2016-02-22	57440.00040	17.559 ± 0.069	1m0-13	R	200
2016-02-23	57441.01024	17.417 ± 0.046	1m0-13	R	200
2016-02-24	57442.00571	17.492 ± 0.047	1m0-13	R	200
2016-02-25	57443.02726	17.485 ± 0.044	1m0-13	R	200

Table A1. Continued.

Date UT	MJD	magnitude (R)	Telescope	Filters	Exposure times (s)
2016-02-27	57445.62117	17.318 \pm 0.053	1m0-03	R	200
2016-02-28	57446.01335	17.420 \pm 0.035	1m0-13	R	200
2016-03-01	57448.06750	17.008 \pm 0.018	1m0-10	R	200
2016-03-01	57448.62489	17.028 \pm 0.021	1m0-03	R	200
2016-03-03	57450.60801	17.112 \pm 0.018	1m0-03	R	200
2016-03-04	57451.60506	17.130 \pm 0.018	1m0-03	R	200
2016-03-05	57452.60201	17.313 \pm 0.021	1m0-03	R	200
2016-03-07	57454.40306	17.337 \pm 0.024	1m0-05	R	200
2016-03-07	57454.62370	17.337 \pm 0.022	1m0-03	R	200
2016-03-09	57456.36274	17.483 \pm 0.023	1m0-05	R	200
2016-03-09	57456.94641	17.457 \pm 0.024	1m0-13	R	200
2016-03-10	57457.58832	17.391 \pm 0.025	1m0-03	R	200
2016-03-11	57458.58716	17.275 \pm 0.020	1m0-03	R	200
2016-03-12	57459.63460	17.106 \pm 0.019	1m0-03	R	200
2016-03-13	57460.74649	16.931 \pm 0.020	1m0-03	R	200
2016-03-14	57461.63193	16.717 \pm 0.014	1m0-03	R	200
2016-03-15	57462.96572	16.552 \pm 0.025	1m0-13	R	200
2016-03-16	57463.93002	16.539 \pm 0.015	1m0-13	R	200
2016-03-17	57464.56933	16.648 \pm 0.017	1m0-03	R	200
2016-03-18	57465.61511	16.686 \pm 0.026	1m0-03	R	200
2016-03-20	57467.91649	17.066 \pm 0.033	1m0-13	R	200
2016-03-21	57468.00108	17.096 \pm 0.025	1m0-10	R	200
2016-03-22	57469.16480	17.188 \pm 0.039	1m0-05	R	200
2016-03-23	57470.15458	17.210 \pm 0.031	1m0-13	R	200
2016-03-24	57471.14439	17.373 \pm 0.049	1m0-13	R	200
2016-03-26	57473.64500	17.209 \pm 0.035	1m0-03	R	200
2016-03-27	57474.74986	17.387 \pm 0.035	1m0-03	R	200
2016-03-28	57475.26752	17.307 \pm 0.033	1m0-05	R	200
2016-03-29	57476.02154	17.393 \pm 0.057	1m0-13	R	200
2016-03-29	57476.37488	17.288 \pm 0.036	1m0-05	R	200
2016-03-30	57477.36813	17.600 \pm 0.040	1m0-05	R	200
2016-04-02	57480.52608	17.793 \pm 0.033	1m0-03	R	200
2016-04-03	57481.13232	17.424 \pm 0.026	1m0-05	R	200
2016-04-03	57481.13548	17.550 \pm 0.030	1m0-05	R	200
2016-04-04	57482.04207	17.424 \pm 0.045	1m0-13	R	200
2016-04-05	57483.51738	15.862 \pm 0.009	1m0-03	R	200
2016-04-07	57485.12103	15.458 \pm 0.007	1m0-05	R	200
2016-04-07	57485.12456	15.460 \pm 0.007	1m0-05	R	200
2016-04-07	57485.14465	15.440 \pm 0.007	1m0-05	R	200
2016-04-07	57485.16703	15.451 \pm 0.007	1m0-05	R	200
2016-04-07	57485.17373	15.451 \pm 0.008	1m0-05	R	200
2016-04-07	57485.34353	15.399 \pm 0.007	1m0-05	R	200
2016-04-07	57485.41653	15.415 \pm 0.007	1m0-05	R	200
2016-04-07	57485.51197	15.424 \pm 0.011	1m0-03	R	200
2016-04-07	57485.51545	15.426 \pm 0.013	1m0-03	R	200
2016-04-08	57486.13174	15.170 \pm 0.007	1m0-05	R	200
2016-04-08	57486.19285	15.132 \pm 0.006	1m0-05	R	200
2016-04-08	57486.86447	15.173 \pm 0.007	1m0-13	R	200
2016-04-09	57487.17049	15.152 \pm 0.006	1m0-05	R	200
2016-04-11	57489.93411	15.247 \pm 0.007	1m0-10	R	200
2016-04-12	57490.49836	15.307 \pm 0.008	1m0-03	R	200
2016-04-13	57491.17433	15.313 \pm 0.006	1m0-05	R	200
2016-04-15	57493.49691	15.665 \pm 0.012	1m0-03	R	200
2016-04-16	57494.16704	15.848 \pm 0.010	1m0-13	R	200
2016-04-18	57496.48241	16.362 \pm 0.017	1m0-03	R	200
2016-04-19	57497.30683	16.587 \pm 0.018	1m0-05	R	200
2016-04-24	57502.85855	17.373 \pm 0.035	1m0-10	R	200
2016-04-24	57502.88819	17.508 \pm 0.046	1m0-13	R	200
2016-04-26	57504.85539	18.029 \pm 0.052	1m0-10	R	200
2016-04-27	57505.50374	17.827 \pm 0.065	1m0-03	R	200
2016-04-27	57505.87528	17.951 \pm 0.046	1m0-13	R	200
2016-04-30	57508.80454	17.788 \pm 0.037	1m0-13	R	200